Digital light processing of high-strength hydroxyapatite ceramics: Role of particle size and printing parameters on microstructural defects and mechanical properties

Digital light processing of high-strength hydroxyapatite ceramics: role of particle size and printing parameters on microstructural defects and mechanical properties

Mehdi Mohammadi, Bartolomeo Coppola, Laura Montanaro and Paola Palmero*

Politecnico di Torino, Department of Applied Science and Technology, INSTM R.U. Lince Laboratory, Corso Duca Degli Abruzzi, 24, Italy

*corresponding author: paola.palmero@polito.it; Department of Applied Science and Technology, Corso Duca Degli Abruzzi, 24, Italy

Abstract

Dense hydroxyapatite (HA) bars are fabricated by Digital Light Processing. The role of *i*) HA mean particle size (MPS), *ii*) the curing depth-to-layer thickness ratio (CD/LT) and *iii*) the debinding process on the printing/debinding flaws and on the flexural strength of the sintered parts are investigated.

A commercial HA was milled for different times to provide powders with MPS from 0.3 to 2.7 μm. Thermal debinding led to delamination and vertical cracks, which decreased by increasing MPS, being 0.9 μm the minimum value to fabricate specimens with appreciable flexural strength. At a given MPS (2.7 μm), CD/LT was varied between 1.4 and 3.3, showing a progressive disappearance of the above major flaws. Finally, the positive effect of water debinding prior to thermal debinding in reducing the crack formation was demonstrated. After optimization, bars achieved a strength > 100 MPa, as the highest value among dense HA fabricated by lithography-based techniques.

Keywords

DLP; Stereolithography; Hydroxyapatite; Particle size; Curing depth; Printing flaws; Flexural strength.

1. Introduction

Advanced oxide ceramics are usually classified into structural and functional ceramics: while the former is characterized by excellent mechanical properties (such as compressive and flexural strength, hardness and wear resistance), the latter typically shows lower mechanical performance but specific functions, due to their tailor-made structure, composition and properties [1].

One of the hurdles to the broader implementation of advanced ceramics is their challenging manufacturing process. Traditional shaping technologies include uniaxial or isostatic pressing, slip/gel casting and injection moulding. Such shaping technologies allow the fabrication of parts with simple geometries and moderate accuracy/precision. In addition, machining of ceramic components is extremely difficult owing to their hardness and brittleness, and this is especially true for larger parts.

The use of 3D printing as a net-shape forming technique for technical ceramics allows the design and fabrications of unprecedented complex three-dimensional shapes, with complicated inner architectures and curved surfaces, with very high precision and accuracy in the fabricated details.

Although different 3D printing techniques have already demonstrated the feasibility in producing advanced ceramics [2-4], stereolithography is the only additive manufacturing technique that allows the fabrication of ceramics with high resolution and surface finishing, and provide the required specification of mechanical and functional properties [4-6]. In this process, the component is obtained through a point-by-point laser polymerization of a liquid photosensitive monomer, filled with a high content of ceramic particles. The subsequent layer by layer photopolymerization allows to build the 3D construct. After printing, parts are submitted to thermal debinding, to eliminate the organic binder, and sintering, to consolidate the ceramic structure. Digital Light Processing (DLP) is a type of stereolithography where the laser is replaced by a UV projector, allowing the photopolymerization of an entire layer at once, making the process faster while assuring the same or even higher printing quality [4]. In spite the key advantages offered by this technology, some issues deserve to be still overcome, especially when the fabrication of dense, structural parts is concerned. Two major flaws arise by this technology: delamination, which means a not perfect joining between consecutive layers, and debinding defects, due to the gas pressure exerted by the volatilized organic fraction during debinding. This last issue is particularly serious for bulk, large parts since the mass transport becomes increasingly diffusion-limited as the features of the component increases in size [7-9], leading to cracks and emphasising delamination.

Calcium phosphates are a type of advanced oxide ceramics, whose fabrication by stereolithography and DLP technologies has already been proven [10-14]. These ceramics are characterized by exceptional biological properties, such as biocompatibility, bioactivity and – for certain compositions – bioresorbability, which arises from the similarity of their chemical composition to the mineral part of human bone [15-17]. These properties make them suitable for use in prosthetic components, especially in orthopaedic [17-19] and dental [20,21] applications. Aimed at mimicking the architecture of cancellous bone, 3D-printed calcium phosphates are shaped as porous/lattice scaffolds, with specific characteristics regarding porosity level, pore and interpore channel sizes to supply proper cell attachment and vascularization. At the same time, scaffolds have to possess enough mechanical strength to structurally support the newly formed tissue. The latest frontier in hard tissue engineering is boosting the development of biomedical devices with either mechanical and functional properties, able to mimic the exceptional structural properties of natural bone, and at the same time displaying the required characteristics of osteoinduction.

In this frame, stereolithography and DLP technologies have been predominantly used to fabricated lattice scaffolds [22-31], and some of them have already tested into *in-vitro* [22-24, 26-28, 29, 31] and *in-vivo* [22,26,28,29,31] experiments. However, a poor attention has been paid to the processing steps, especially to the optimization of the slurry, with very few papers dedicated to the fabrication of dense parts [11,32], whose mechanical validation is the basis for the development of further porous and complex shapes.

Therefore, the aim of this work is to investigate the role of slurry processing and printing parameters on the fabrication of 3D printed dense hydroxyapatite structures by DLP technique. To this aim, several parts obtained by slurries made by hydroxyapatite powders at different particle size distributions are printed, while the curing depth-to-layer thickness ratio was varied in a precise range. The evolution of usual defects of lithography-fabricated ceramic parts by changing the starting particle size and curing depth is here investigated as never performed for hydroxyapatite ceramics, thus filling an important literature gap and providing a scientific advancement for the DLP-fabrication of high-strength hydroxyapatite parts.

2. Materials and methods

2.1 Materials

A commercial hydroxyapatite (HA) powder (Captal R, supplied by Plasma Biotal, UK) was used as starting material. According to the supplier, the powder is a high purity powder classified as

biomedical grade HA meeting the requirements of ISO 13779-6 2015. The Ca/P molar ratio of the powder was determined by a semi-quantitative XRD method proposed by Raynaud et al. [33] described in the authors previous article [34].

For slurries preparation, a commercial photocurable resin (ADMATEC Europe BV, The Netherlands) was used. The DTA-TG curves of the polymerized resin depicted in **Figure 1** are used to identify the temperature regions where rapid mass loss occurs. It can be seen that the organic binder is removed below 500 °C with two main mass removal events. The first slight mass loss (~ 4.4%) from room temperature to about 150°C, while most of the mass loss (87.3%) occurred from about 270 °C to 480 °C. On the ground of the resin thermal behaviour, the debinding cycle was established, as reported in Section 2.4.

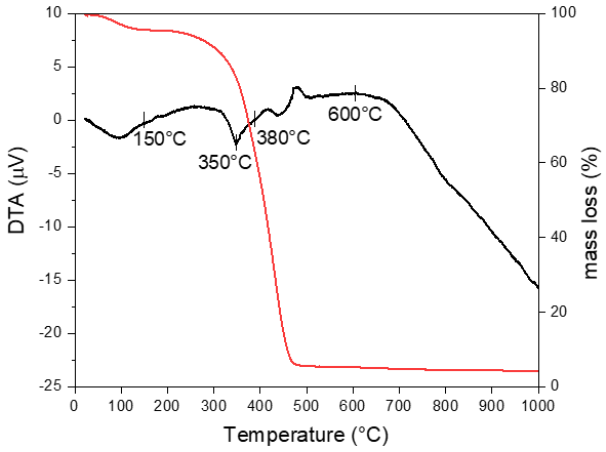

Figure 1: DTA-TG of the photopolymerized resin.

A commercial dispersant (Disperbyk-103, BYK Chemie, Germany) was employed to optimize the solid loading and improve the wettability of the ceramic powder by the resin.

2.2 Slurries preparation

HA powder was dispersed by ball-milling, carried out in distilled water, using 2-mm zirconia spheres as milling media, and using powder-to-sphere weight ratio of 1:6. Ball-milling was carried out at a fixed speed for different times, up to 48 h, to achieve the desired particle size distribution, with mean particle size (MPS) ranging from about 0.26 µm to 2.65 µm.

Slurries were prepared using both as-received and ball-milled powders. Slurries are labelled according to the mean particles size of the employed powder for slurry preparation, as HA-MPS.

For example, HA-0.3 label designates the slurry prepared starting from the powder milled to achieve an MPS of 0.26 μm. Samples designation is collected in **Table 1**.

All the slurries were prepared with the aim to maximize their solid loading at the given HA particle size. For this reason, the dispersant amount, which varied in the range 7-10 wt% as respect to the dried powder, was tuned in each specific formulation. The slurries were prepared according to the following procedure. First, slurries were prepared at ~ 60 wt%, with at least 4 wt% of dispersant, and mixed by planetary milling at 400 rpm for 3 h using agate spheres (∅ = 10 mm). Then, additional powder and extra dispersant were step by step added, each step followed by 10 min milling, and rheology characterisation of the slurry. The following additions continued up to achieve the maximum solid loading at acceptable rheological behaviour. All slurries were deaired under vacuum for 120 min before printing. Solid loading and dispersant amount of each slurry are collected in **Table 2**.

2.3 Printing

Bars (as-printed dimensions: 32 x 3 x 4 mm - L x T x H) for three-point bending tests were designed using the AutoCAD software.

Specimens were printed using a DLP-based stereolithographic device (ADMAFLEX 130, ADMATEC Europe BV, The Netherlands). The machine works with an adjustable tape transport speed from 10 to 20 mm/s on which the photocurable slurry is spread by a doctor blade with a gap size of 125 μm. Considering shear as the relative motion between adjacent layers of a moving liquid, shear rate (τ) can be calculated using the following formula:

$$\tau = \frac{V}{h} \qquad (1)$$

where V is the velocity of the relative motion and h is the slurry thickness. So, the applicable shear rate of our printing jobs is calculated between 80 to 160 s^{-1}. The main printing parameters, including exposure time and LED power, were optimised to achieve a good printing quality, also following Authors' previous studies [35,36].

In a first set of experiments, samples were printed starting from slurries prepared at different MPS, from the finest (0.26 μm) to the largest (2.65 μm) particle size. Samples were printed by setting the layer thickness to 40 μm, and the curing depth-to-layer thickness ratio (CD/LT) to 2.0. As finer particles increase the scattering of the UV light, the other printing parameters (energy dose and exposure time) were accurately adjusted to achieve the same CD in the different slurries [37]. The attenuation of energy due to the resin is given by the Beer-Lambert law:

$$E_z = E_0 \exp\left(\frac{-z}{D_p}\right) \qquad (2)$$

where E_0 is the energy dose at the surface of printing layer, z is the depth beneath the surface (irradiation depth) and D_p is the depth of penetration inside the resin [38,39]. According to eq. (2), the energy dose at depth z (E_z) is reduced exponentially with distance from the surface. It is also shown that this attenuation of energy is higher at higher energy doses [38]. Different energy doses in different depth results in different polymerization level and therefore could be a source of microstructural defects due to residual stresses.

In a second experimentation, slurries were prepared at the same MPS (2.65 μm), while samples were printed at different CD/LT, to investigate the role of this parameter on printing defects and samples mechanical strength.

2.4 Debinding and Sintering

As-printed samples were debinded using two different procedures. In one case, samples surfaces were rinsed with deionized water to remove extra slurry from the surface, while in the second case, as-printed samples were submitted to a water debinding step, before the thermal one. Precisely, samples have been soaked in deionized water at approx. 40 °C for 24 h to remove uncured slurry. Then, samples were dried carefully at room temperature for 1 night, followed by oven drying at 70 °C for 6 h. Finally, both the debinded samples typologies were submitted to a thermal debinding step up to 600 °C, performed according to the cycle depicted in **Figure 2**, and established on the ground of the DTA-TG curve of the neat polymerized resin (see Figure 1).

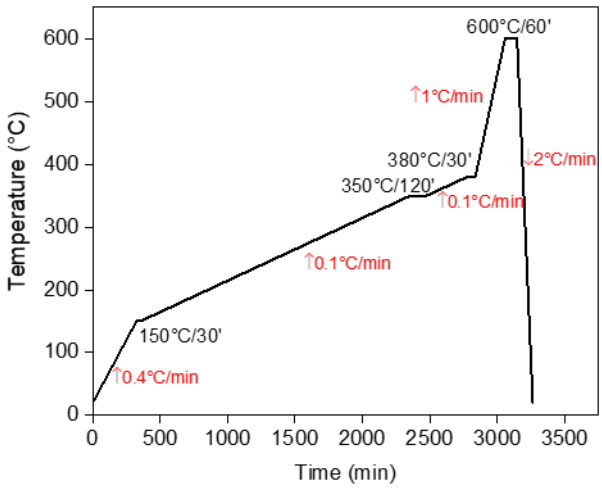

Figure 2: Thermal debinding cycle used for the printed samples

Debinded samples were placed into furnaces (Carbolite 1800 electric furnace, Carbolite Gero GmbH) and sintered at 1200 °C or 1300 °C (depending on the MPS) for 1h. Precisely, the heating rate was 10°C/min up to 1000°C, and then at 5 °C/min up to 1200°C or 1300 °C, followed by a cooling step at 10°C/min till room temperature. The change in heating rate from 10 °C/min to 5 °C/min was established on the ground of an authors' previous work [40].

2.5 Powders, slurries and samples characterization

The particle size distributions of the powders during ball-milling were determined by laser granulometry (Laser Particle Sizer Analysette 22; Fritsch, Idar-Oberstein, Germany).

The phase composition was analysed by X-Ray Diffraction (XRD Philips PW 3800) in the 2θ range 5-70°, with a step size of 0.026° and an acquisition time per step of 5 seconds.

The temperature region of resin mass loss was determined by Thermogravimetric-Differential Thermal analyses (TG-DTA, LabSys evo machine, Setaram), performed at 10°C/min with a N_2 flow rate of 20 ml/min.

The rheological behaviour of the slurries was investigated using a rotational rheometer (Kinexus Pro+, Netzsch Geraetebau GmbH, Selb, Germany) equipped with stainless steel roughened parallel plates (20 mm diameter) having a gap between plates of 1 mm.

The geometric density of the green and sintered samples was determined by mass and geometric measurements. The density of the sintered samples was also determined by Archimedes' method; these densities were related to the theoretical values by considering a HA theoretical density of 3.156 g/cm^3 (JCPD file n. 01-072-1243).

The microstructural characterization of the sintered materials was performed by a field emission scanning electron microscope (FESEM, Zeiss Supra 40, Jena, Germany), and performed on polished and thermally etched surfaces. The grain size of the sintered microstructures was determined by image analysis (Scandium software) of the FESEM images.

Flexural strength was determined by 3-points bending tests using an electromechanical testing system (Zwick Roell 2014, Ulm, Germany) equipped with a load cell of 50 kN. Sintered prismatic samples (25 x 2 x 3 mm - L x W x H) were tested with a crosshead speed of 100 µm/s and a support span of 18 mm. Samples submitted to mechanical characterization were as-printed, without any preliminary grinding and polishing steps, to exploit the ability of DLP in providing high-surface quality to the samples.

3. Results and discussion

3.1 Powders characterization and dispersion of powders

The XRD pattern of the as-received powder is depicted in **Figure 3**. According to the JCPD file n. 01-072-1243 all the peaks can be identified as belonging to the hydroxyapatite phase, with hexagonal lattice structure. The powder is also characterized by a Ca:P ratio of 1.67, which provides stoichiometric HA. Calcination of the powder at 1000 °C for 15 hours [33,34] showed no phase transformations, indicating a high thermal stability of HA, able to provide final samples free from any secondary phases (results not shown).

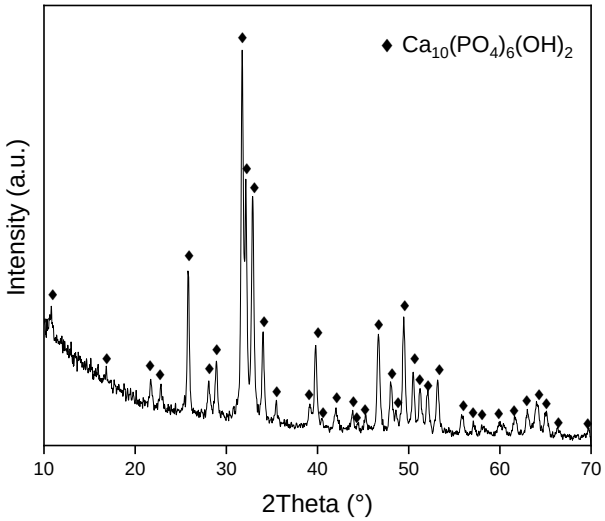

Figure 3: XRD patterns of as-received HA. All marked peaks correspond to hydroxyapatite phase, according to JCPD file n. 01-072-1243

In **Figure 4 (a)**, a FESEM micrograph of the as-received powder is depicted, showing the presence of micronic-size agglomerates, made by ultrafine particles, as highlighted in the higher magnification image **(b)**. The size of primary particles ranged between 250 and 400 nm, and were characterized by acicular morphology, as characteristic of hydroxyapatite powders [41].

Concerning the particle size distribution, as-received HA was characterized by a bimodal distribution (**Figure 5,** black curve), with a D_{50} value of 2.65 μm (**Table 1**). Powders milled for 1.5 to 8 h were still characterized by bimodal distributions, where the intensity of the peak located at lower particle size progressively increased by increasing the milling time. Powders milled for 24 and 48 h achieved a narrow, monomodal distribution, with the 48-h milled powder achieving the lowest MPS (0.26 μm). In **Table 1**, the values corresponding to 10, 50 and 90% of the cumulative distributions are collected. Samples designation refers to the D_{50} values (rounded to the first decimal number), as shown in Table 1.

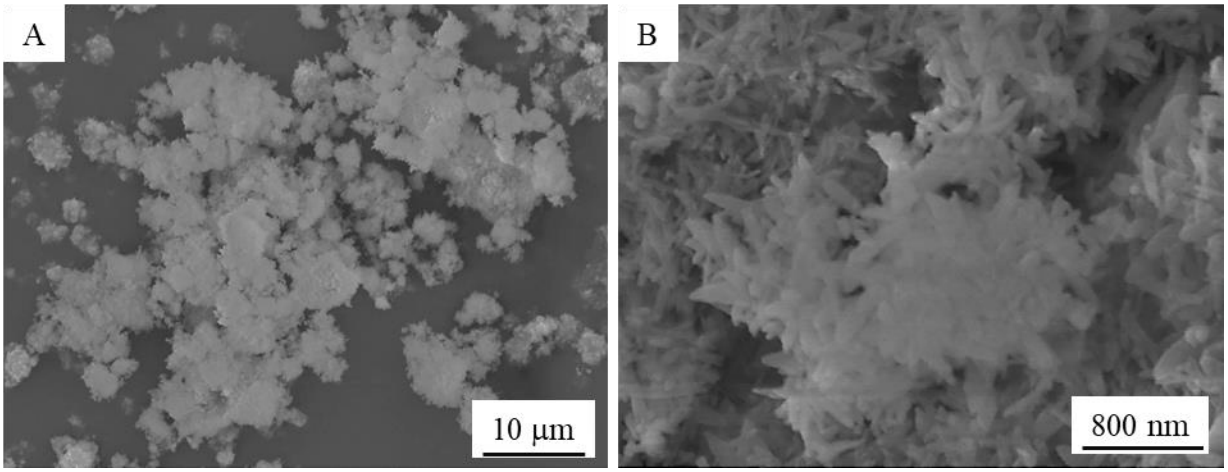

Figure 4: FESEM micrographs of the as-received powder, at lower (a) and higher (b) magnifications

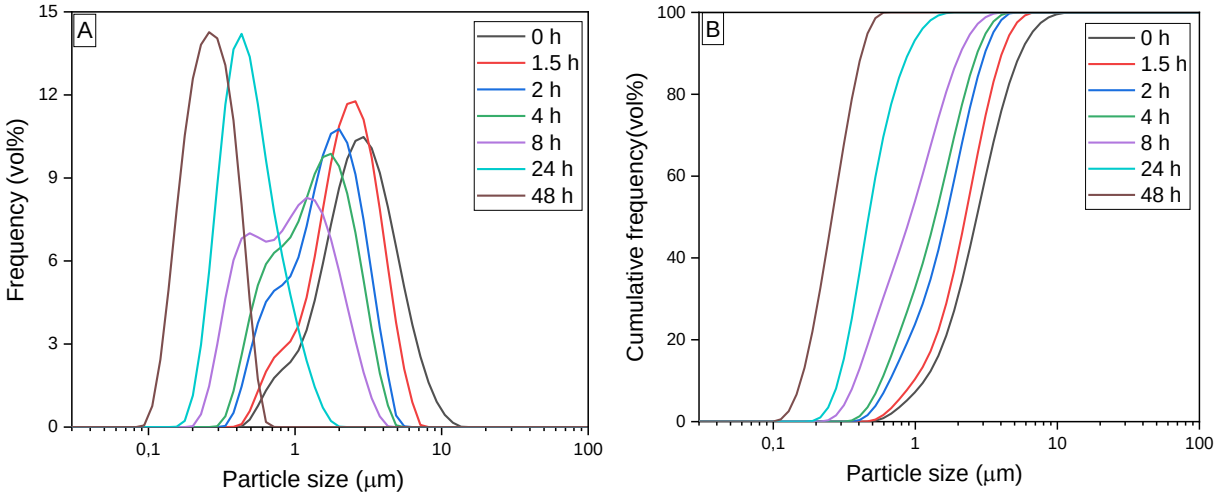

Figure 5: particle size distribution as frequency (a) and cumulative frequency (b) of HA powder, at different ball-milling times.

Table 1: D_{10}, D_{50} and D_{90} values of HA powder milled for different hours

Powder designation	Milling time (h)	D_{10} (µm)	D_{50} (µm)	D_{90} (µm)
HA-2.7	0	1.16	2.65	5.52
HA-2.3	1.5	0.98	2.25	4.08
HA-1.7	2	0.66	1.65	3.09
HA-1.4	4	0.58	1.38	2.73
HA-0.9	8	0.39	0.91	2.09
HA-0.5	24	0.29	0.50	0.96
HA-0.3	48	0.16	0.26	0.41

3.2 Slurry preparation based on rheological behaviour

High solid loading is a prerequisite to manufacture dense ceramic parts, which helps to achieve low and uniform shrinkage during sintering and to avoid cracks and defects formation especially during binder removal. To this aim, it is deemed necessary to achieve HA-resin slurries with the highest possible solid loadings along with appropriate rheological behaviour for each starting powder.

Figure 6 (a) shows the shear viscosity as a function of shear rate for the slurries made from HA-0.3, as the finest particle size achieved by ball milling for 48 h. Initial slurry composition, with solid loading of 61 wt% at 4 wt% dispersant, showed a shear-thinning behaviour, with a marked viscosity decrease as the shear rate increases (light blue curve). In fact, as the level of shearing stress is gradually increased, the structural units respond to the applied stress by aligning themselves in the direction of flow which facilitates bulk flow in the system [42]. Such behaviour is the one required in the stereolithography process, as it assure the slurry being spread on the tape evenly [43]. However, keeping the same dispersant-to-solid amount ratio in increased solid loading slurries resulted into an expected increase in viscosity (data not shown), as the inner friction due to HA particles increased. Therefore, an increased dispersant amount was needed to achieve the same viscosity [27]. The stepwise addition of +1% dispersant allowed to increase the solid loading up to 64% (green curve), then to 68 wt% (blue curve, with further +2% dispersant) and finally to 69 wt% (dark blue curve), achieved with a final dispersant amount of 8%. In this way, almost superimposable curves were obtained, especially in the range between 80 and 160 s^{-1} shear rates, which corresponds to our printing conditions. In literature, different viscosity values are regarded as acceptable upper limit viscosity for the stereolithography of ceramics. Some of these values that resulted in successful stereolithographic printings are 3 Pa·s at the shear rate of 10 s^{-1} [44] and 30 s^{-1} [45], 1.7 Pa·s at shear rate of 150 s^{-1} [46] and 3.7 Pa·s at a shear rate of 10 s^{-1} [32]. While these values are close to each other, the variation can be attributed to the different printing equipment used with different specifications. However, it seems that the viscosity of 5 Pa·s at the working shear rate can be properly considered as the upper limit [47-49]. In our system, the reference shear rate, corresponding to the shear rate applied by the blade on the slurry during its spreading, was identified at 100 s^{-1}, providing shear viscosity of 3.1, 3.4, 3.6 and 4.6 Pa·s for the four slurries in Figure 6 (a) at increasing solid loadings. Although all the slurries showed viscosity lower than the limit value, that of the most charged formulation was very close to the threshold, indicating that the maximum solid loading was already achieved. Needless to say that increasing the dispersant content to more than 8%, didn't reduce the viscosity in the latter slurry.

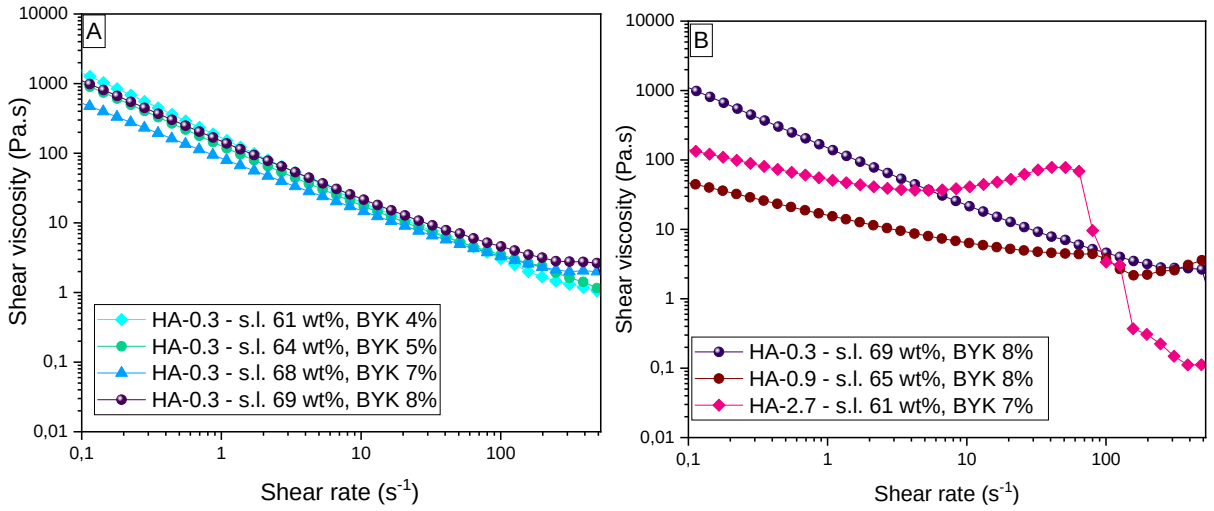

Figure 6: Rheological curves of: **(a)** HA-0.3 slurries at increasing solid loadings (s.l.) and dispersant (BYK) amount; **(b)**: HA-0.3, HA-0.9 and HA-2.7 slurries at their optimized solid loading/dispersant amount

By increasing the MPS of the HA powder, the optimization of the slurries became more challenging. HA-0.5 was still prepared at 69 wt%, with the same dispersant amount (8%) used for HA-0.3. However, by further increasing the MPS, it was necessary to reduce the solid loading to achieve good flowability. In fact, the solid loading was reduced to 65 wt% for HA-0.9, HA-1.4, HA-1.7 and HA-2.3 slurries, and finally to 61wt% for HA-2.7 (**Table 2**). In addition, significant differences were observed in the rheological behaviour of slurries prepared by powders at different MPS. An example is provided in **Figure 6 (b)**, which compares the shear viscosity of HA-0.3, HA-0.9 and HA-2.7 slurries. At low shear rates, HA-0.3 shows a significantly higher shear viscosity compared to the other two slurries, which can be easily imputed to its higher solid loading and finer particles, producing higher frictional resistance from relative motion between particles [43]. In addition, HA-0.3 presents a shear thinning behaviour in the whole range, as previously described. HA-0.9 and HA-2.7 have significant lower viscosities at low shear rates, and a tendency towards a Newtonian behaviour. Indeed, HA-0.9 presents a moderate shear thinning behaviour up to ~ 150 s^{-1}, where viscosity increased again, showing shear thickening behaviour. On the contrary, HA-2.7 presents an almost Newtonian behaviour in the range 0.1 – 90 s^{-1} followed by an abrupt viscosity decrease. In spite anomalous, a similar behaviour was already observed in literature. Knowles et al. [41] investigated three types of HA particles characterized by acicular morphology, as in our case, and studied the effect of HA particle size and distribution on the rheological behaviour (study limited to the 10-50 s^{-1} shear rate range). Authors found that the formulation prepared using HA at the wider particle size distribution showed a Newtonian behaviour, while the other formulations, prepared with powders having a narrower particle size distribution show a shear-thinning

behaviour. Similarly, HA-0.3 has a monomodal and narrow particle size distribution while HA-0.9 and HA-2.7 show bimodal distributions (Figure 5). It should be also pointed out that the same paper addressed the key role played by the dispersant amount on the slurry rheological behaviour, highlighting the need to optimize it for each single formulation, at specific particle size distribution.

Although the different rheological behaviours, at the shear rate reference value (100 s^{-1}) the three slurries showed similar shear viscosity, precisely 4.7, 4.0 and 3.5 Pa·s for HA-0.3, HA-0.9 and HA-2.7 slurries, respectively, being all these values below the threshold [49] to achieve good printability. A summary of slurry parameters, according to starting MPS, is presented in **Table 2**.

Table 2: solid loading and dispersant amount, as optimized for each slurry

Slurry designation	Solid loading* vol%	Solid loading* wt%	BYK** wt%
HA-0.3	43	69	8
HA-0.5	43	69	8
HA-0.9	39	65	8
HA-1.4	39	65	10
HA-1.7	39	65	10
HA-2.3	39	65	9
HA-2.7	35	61	7

*Dispersant amount is considered in the calculation of solid loading
**BYK amount is calculated respect to the dry powder

3.3 Set-up of printing, debinding and sintering conditions

Slurries produced by powders at different MPS were printed. In a first attempt, HA-0.3, HA-0.5, HA-0.9, HA-2.3 and HA-2.7 were selected in order to investigate the role of MPS on sintering behaviour, microstructural development and mechanical strength. In all cases, the layer thickness was fixed to 40 μm, and the curing depth-to-layer thickness ratio (CD/LT) was set to 2.0.

The as-printed samples showed a regular shape without any deformation or warping, and also no visible delamination between layers was detected. As an example, in **Figure 7** (a) an as-printed sample (grey bar) from the HA-0.3 slurry is depicted.

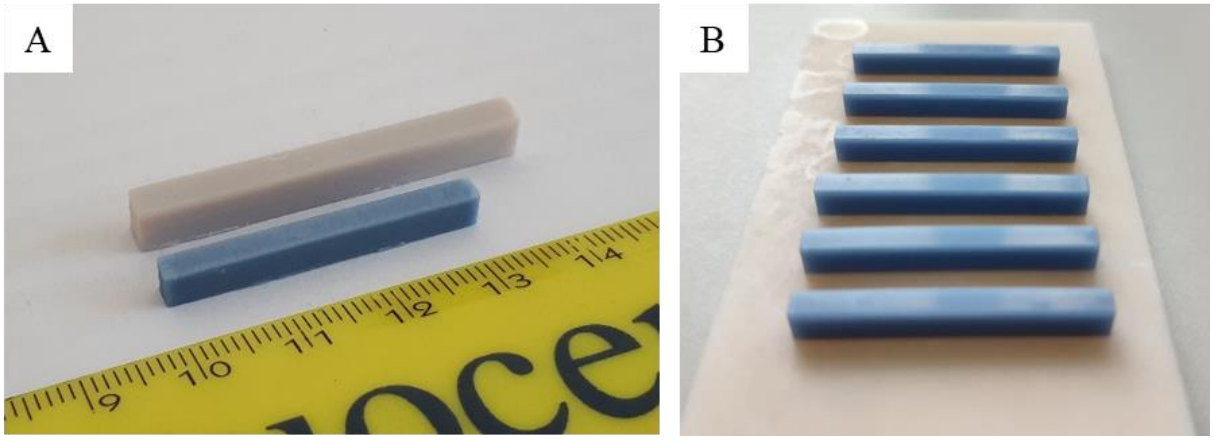

Figure 7: Photographic image of: (a) as-printed (grey) and sintered (blue) bars produced by HA-0.3; (b) sintered bars produced by HA-2.7

Samples were then submitted to thermal debinding, according to the thermal cycle shown in the Experimental section. FESEM observations of the cross-sections of as-printed and thermally debinded bars derived by powders at finest (HA-0.3) and largest (HA-2.7) MPS are depicted in **Figure 8**. Both as-printed samples present a fully compact structure, almost free from defects (Figs. a and e). However, when thermally debinded sections are concerned a clear difference between the two samples was easily observed (Figs. b and f). In fact, while HA-2.7 maintained a fully compact microstructure, with just few short horizontal cracks, HA-0.3 presents numerous horizontal cracks characterized by vertical jogs, with jogs displacements larger than the layer thickness [7].

The higher magnification micrographs of the thermally debinded samples (Figs. c and d for HA-0.3; Figs. g and h for HA-2.7) highlighted a further difference. The microstructure of HA-0.3 appears to be highly homogeneous, and made by closely packed ultrafine HA particles. On the opposite, a less homogeneous microstructure with micronic-sized agglomerates can be observed in HA-2.7. Here particles seem to form less-packed structure, being this effect imputable to either the higher particle/agglomerate size and lower solid content of HA-2.7 slurry compared to HA-0.3. Anyway, these results prove the effective de-agglomeration of the starting powder by ball-milling, being the very fine dispersion maintained once the dispersed powder was added to the resin.

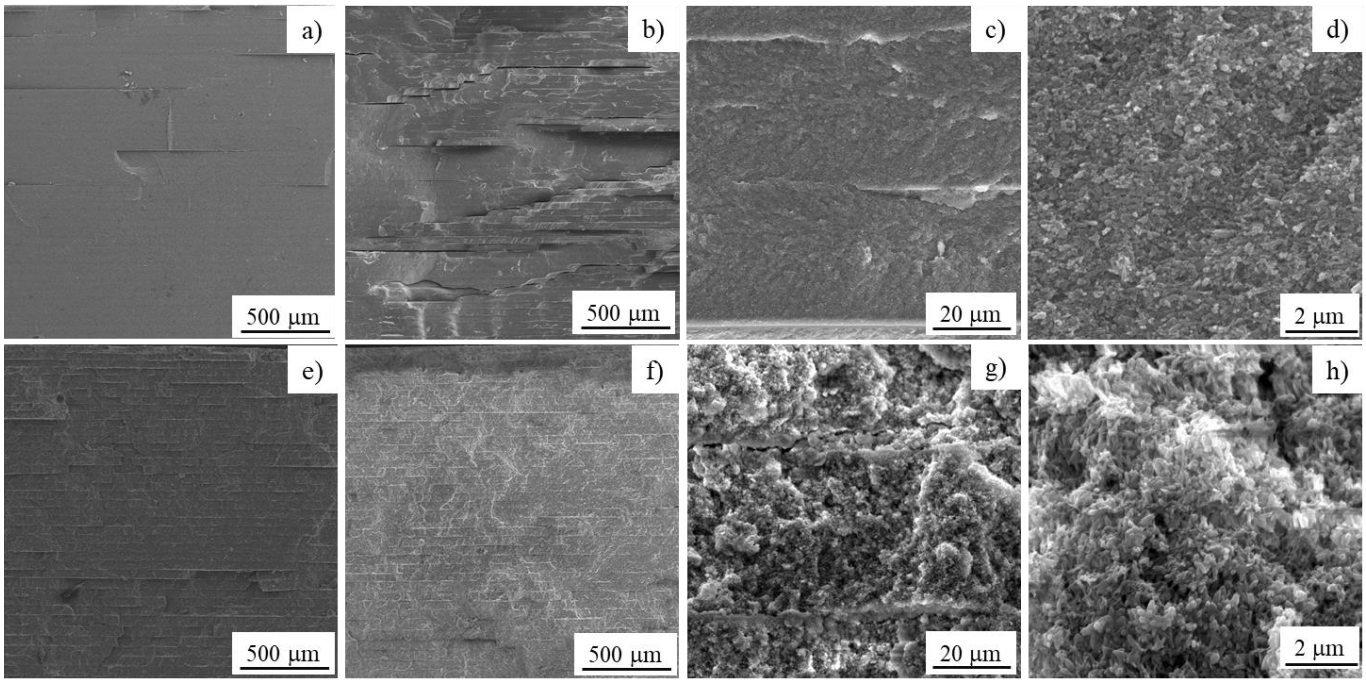

Figure 8: FESEM micrographs of HA-0.3 (a-d) and HA-2.7 (e-f) cross-sections. As-printed state (a,e) and thermally debinded state, at different magnifications (b-d and f-h).

The above results suggest a key role played by MPS on printing flaws. To perform a systematic investigation, bars produced by powders at the five different particle sizes were sintered, being the sintering temperature (1200°C or 1300 °C) selected to achieved a final density (as determined by the Archimedes' method) higher than the target value of 95%, according to a previous work [34]. Sintering was accompanied by a high linear shrinkage. In fact, considering the shrinkage in the length direction, it was about 21.5% for HA-0.3 (at the finest MPS and highest solid loading) and around 27% for HA-2.7 (at the largest MPS and lowest solid loading). In spite large, no visible deformation or warping occurred during sintering, as shown in Figure 7 for both HA-0.3 (a) and HA-2.7 (b) sintered bars. Sintering cycle, green and final density, as determined by both Archimedes' and geometrical measurements are depicted in **Table 3**. We can observe that the green density decreased by increasing the MPS, in line with the decrease of solid loading (see Table 2). Archimedes' densities were high for all the investigated slurries, in the range 98.0-98.9%, indicating the suitability of the adopted sintering cycles. FESEM observations performed on polished and thermally etched surfaces showed highly dense and homogeneous microstructures, in lines with the Archimedes' density values. An example is provided in **Figure 9** for HA-0.3 and HA-2.7: in spite of the significant difference in final grain size, being HA-0.3 characterized by fine particles (average size of 1.24 ± 0.49 µm) and HA-2.7 by larger grains and wider size distribution (3.87 ± 1.54 µm), both samples showed highly sintered microstructures, with very limited residual closed porosities.

Table 3: Sintering cycle, green and sintered density, and flexural strength of printed bars, all printed at CD/LT = 2.0

Slurry designation (wt%)	Sintering cycle	Green density* (g/cm^3)	Sintered density** (% TD)	Geometrical density (%TD)	Flexural strength (MPa)
HA-0.3	1200 °C/1h	2.03 ± 0.01	98.3 ± 0.5	91.0 ± 1.4	n.d.
HA-0.5	1200 °C/1h	2.02 ± 0.01	98.9 ± 0.1	91.5 ± 0.8	n.d.
HA-0.9	1300 °C/1h	1.95 ± 0.02	98.0 ± 0.1	93.5 ± 0.6	47 ± 6
HA-2.3	1300 °C/1h	1.98 ± 0.02	98.8 ± 0.3	94.5 ± 0.6	60 ± 7
HA-2.7	1300 °C/1h	1.83 ± 0.03	98.0 ± 0.6	94.4 ± 0.9	87 ± 9

*green density is intended as as-printed density (= resin and powder)
**Sintered density is referred to theoretical density of HA equal to 3.156 g/cm^3

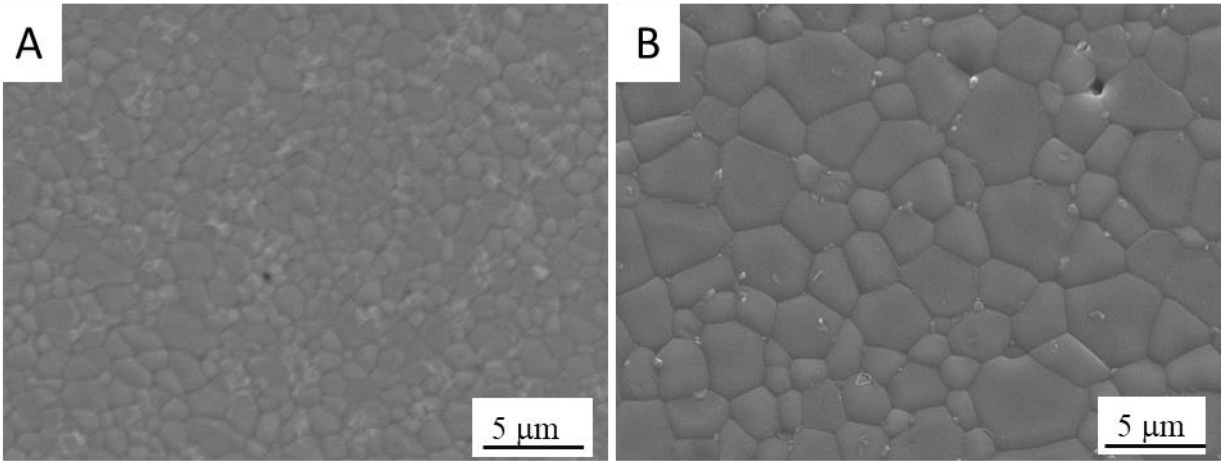

Figure 9: FESEM micrographs of HA-0.3 (A) and HA-2.7 (B) sintered samples

However, geometrical densities supplied much lower values compared to Archimedes' ones, especially for the samples printed by the slurries at the lowest MPS. As the buoyancy method implies the water infiltration inside the open porosities and flaws, it can result in overestimation of the actual densities [50]. Thus, the difference between Archimedes' and geometrical density suggests the presence of flaws and delamination in the printed samples, which is reasonable considering the cross-section observations performed on the thermally debinded HA-0.3 and HA-2.7 samples shown in Figure 8. It can be also observed that the discrepancy between Archimedes and geometrical densities progressively reduced by increasing the MPS, suggesting fewer defective structures. To support this hypothesis, FESEM observations were systematically performed on the polished cross sections of all the sintered samples, as shown in **Figure 10**.

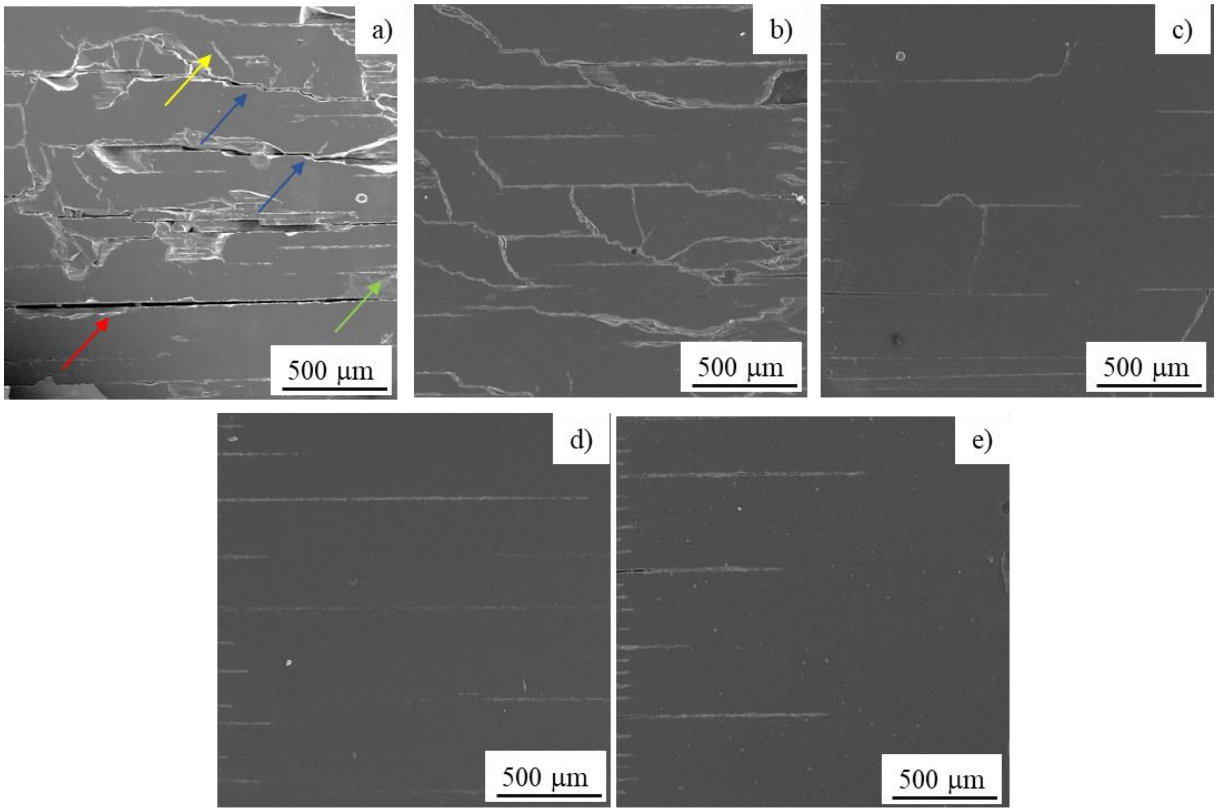

Figure 10: FESEM micrographs of the polished cross-sections of samples HA-0.3 (a), HA-0.5 (b), HA-0.9 (c), HA-2.3 (d) and HA-2.7 (e).

HA-0.3 cross section, Figure 10 (a), revealed a number of flaws, moving in parallel and vertical directions respect to the printing direction, and corresponding to those already observed in the thermally debinded state (Figure 8b), but with larger extension and thickness. Also, the presence of vertical/complex cracks seems increased compared to the green state. The arrows in the figure highlight the four different types of flaws recognized: delamination (red arrow), horizontal/stepped cracks (blue arrows), vertical crack (yellow arrow), and edge cracks (green arrow). Even if horizontal cracks and delamination are normally not discerned, as both denote a not sufficient layer integration, a distinction is here proposed: delamination is intended as a deep and thick crack separating two different layers, whose thickness typically decreased while moving inside the ceramic body; horizontal cracks are intended as thinner cracks, frequently characterized by vertical jogs, also here defined as ‘stepped’ cracks.

When moving to sintered samples derived by higher MPS slurries, a significant reduction of the flaws can be clearly observed. HA-0.5 showed the same types of defects as HA-0.3, even if in a reduced amount. In particular way, delamination decreased, while edge and vertical cracks were still frequently observed, as well as the stepped horizontal cracks. An even better situation was observed in HA-0.9. Thick and long delamination almost disappeared, vertical cracks decreased in

number, and the path of horizontal cracks became more linear. Very similar observations can be found in HA-2.3 and HA-2.7 materials, in which the stepped horizontal cracks completely disappeared, replaced by linear-path cracks.

Delamination and horizontal cracks are typically imputed to the layered fabrication [9]: as a proof, we can see that - under the adopted printing conditions where CD/LT was set to 2 - these flaws can be reduced by using larger HA particles, but not completely eliminated. According to Johansson et al. [8], an increase of CD/LT from 2 to 3 allowed to decrease delamination: this strategy was also explored in this research, and results reported in the next section. At the same time, vertical cracks are usually imputed to the stiffness of the resin [8,9]. A possible solution is to add a plasticizer to the acrylic resin, being its effect on the elimination of intra-laminar cracks already proven in literature [8]. Anyway, independently of the specific crack origin, the key role played by the slurry particle size on the whole flaws pattern is here clearly demonstrated. It is reasonable to assume that organic matter burn-out was more difficult in nanometric-grained structures, characterized by fine interparticle spaces, and high solid loading. In fact, debinding is the most critical and time-consuming step in ceramic stereolithography and often source of cracks [8,53]. Evaporation of a high amount of binder available in the slurry is a complex process and the transport of a large mass of debinding products is diffusion-limited. Accumulation of debinding gases within the ceramic body, if the volatile products do not have time to diffuse out from the structure, leads to pressure build-up and to the formation of cracks or layer delamination [7,54]. As already shown in Figure 8, which compares the as-printed microstructure of HA-0.3 (Fig. 8d) and HA-2.7 (Fig. 8h), by increasing the starting ceramic particle size, the interparticle space increase. These bigger interparticle spaces facilitate a smoother removal of the binder decomposition products throughout the dense body and therefor reduce the associated microstructural damage.

The comparison between the cross-sections of samples HA-0.3 and HA-0.5, which were obtained by slurries at the same solid loading but different particle size, strengthens that the finer the particles, the thicker and more extended the cracks. This finding is in line with a previous report by Johansson et al. [8] where the debinding process of alumina bodies was modified by the addition of non-reactive polymers with low debinding temperature to the slurry formulation. The non-reactive components debinded in advance of the main binder system and introduced free spaces that facilitated the diffusion of further decomposition products, thus reducing both delamination and intra-laminar cracks.

Samples produced by HA-0.3 and HA-0.5 showed a significant brittleness, making difficult their manipulation. On the contrary, starting from HA-0.9, samples could be easily handled, and

therefore were submitted to mechanical tests. Results, depicted in **Table 3**, show a progressive increase of the flexural strength by increasing the MPS: in fact, values increased from 47 to 62 MPa moving from HA-0-9 to HA-2.7.

3.5 Role of CD/LT and water debinding on physical-mechanical properties

Further tests were carried out by using HA-2.7, which showed a less defective cross-section and good mechanical values. In particular way, the impact of a wide range of CD/LT values on the flaws and flexural strength were explored. Also, the effect of the addition of a water debinding step in advance to thermal debinding was studied (**Table 4**).

Table 4: green, sintered density and flexural strength of HA-2.7 printed bars, at different CD/LT values and debinding conditions

Slurry designation	CD/LT	Green density* (g/cm^3)	Archimedes density** (% TD)	Geometrical density** (%TD)	Flexural strength (MPa)
HA-2.7 Thermal debinding	3.4	1.82 ± 0.01	98.0 ± 0.5	92.5 ± 1.3	17 ± 10
	3.0	1.83 ± 0.02	97.9 ± 0.6	93.1 ± 0.9	29 ± 12
	2.6	1.83 ± 0.02	97.9 ± 0.7	93.7 ± 0.8	73 ± 12
	2.3	1.84 ± 0.03	98.0 ± 0.4	94.5 ± 0.8	35 ± 11
	2.0	1.83 ± 0.03	98.0 ± 0.6	94.4 ± 0.9	87 ± 9
	1.8	1.83 ± 0.02	97.8 ± 0.5	94.5 ± 0.9	50 ± 11
	1.6	1.84 ± 0.03	97.8 ± 0.6	94.7 ± 0.8	32 ± 14
	1.4	1.84 ± 0.02	98.8 ± 0.4	94.7 ± 0.8	75 ± 11
HA-2.7 Water & thermal debinding	2.0	1.64 ± 0.01	98.0 ± 0.5	95.5 ± 0.6	62 ± 8
	1.8	1.64 ± 0.02	97.8 ± 0.6	96.5 ± 0.5	85 ± 7
	1.6	1.64 ± 0.01	97.9 ± 0.5	96.9 ± 0.6	97 ± 9
	1.4	1.65 ± 0.02	97.8 ± 0.5	96.8 ± 0.5	96 ± 8

*green density is intended as as-printed density (= resin and powder)
**Archimedes and geometrical densities are referred to theoretical density of HA equal to 3.156 g/cm^3

With reference to the samples submitted to only thermal debinding, we can observe that the CD/LT ratio played a not relevant role on the green density, and a clear correlation between the same parameter and the Archimedes' sintered density could not be stated. However, if the geometrical density is considered, we can observe a certain relation, with the increase of geometrical density values while decreasing CD/LT (**Figure 11a**), suggesting fewer open flaws in samples printed at

lower CD/LT. A systematic observation carried out on polished cross-sections confirmed this result, as we can observe in **Figure 12**.

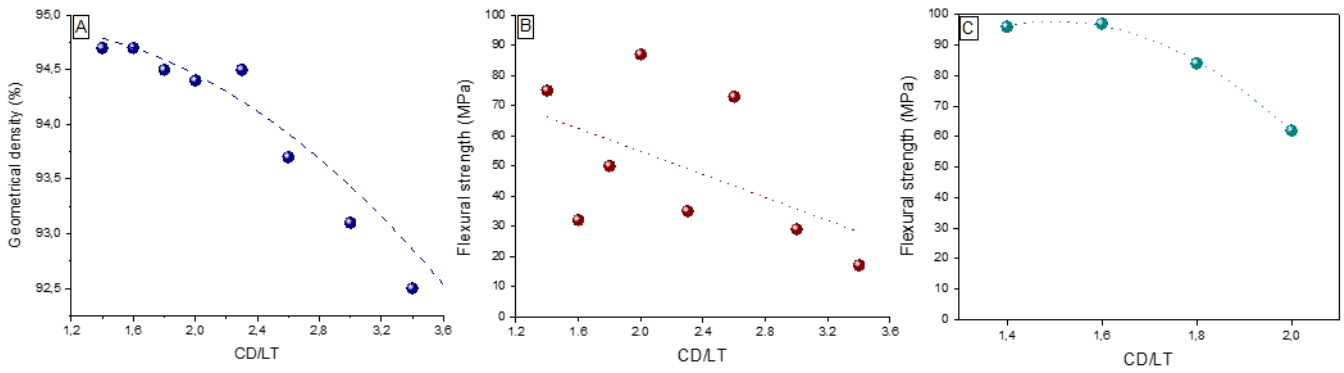

Figure 11: Geometrical density (a) and flexural strength (b) as a function of CD/LT for samples thermal debinded; (c) flexural strength as a function of CD/LT for samples water & thermal debinded.

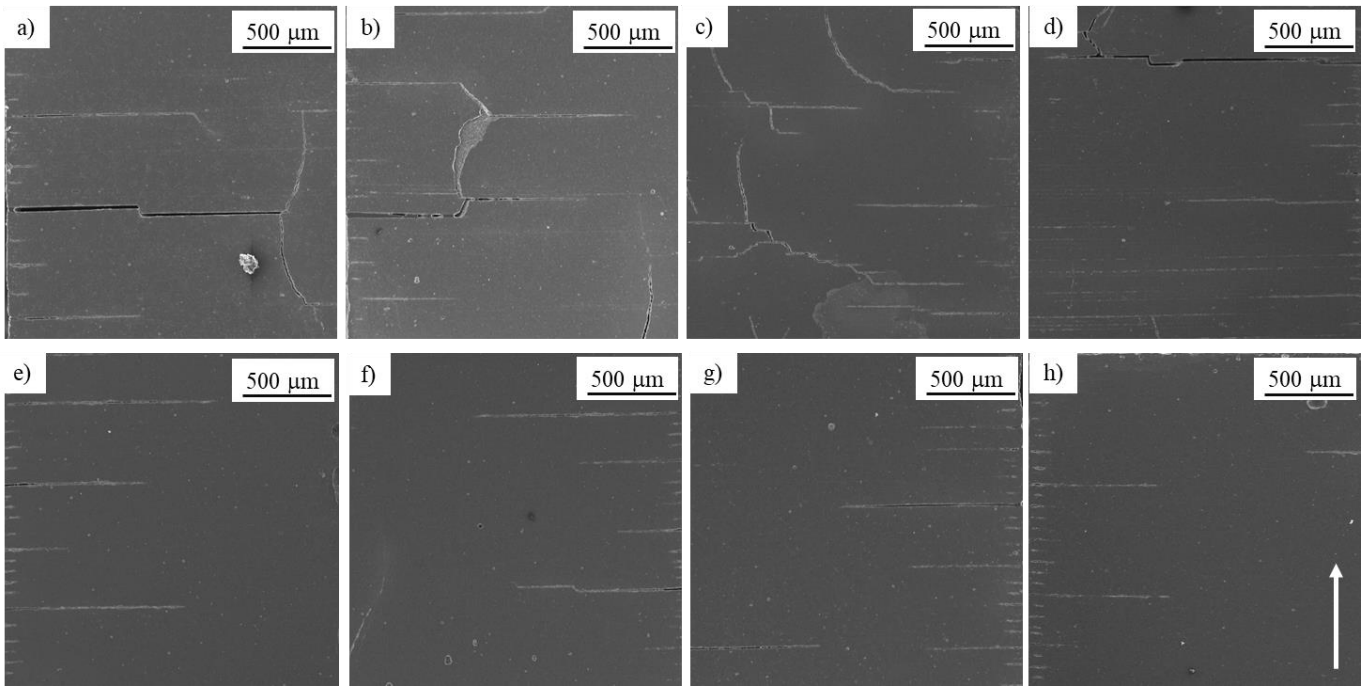

Figure 12: FESEM micrographs of the polished cross sections of samples HA-2.7 (no water debinding) printed at different CD/LT, and precisely: (a) 3.4; (b) 3.0; (c) 2.6; (d) 2.3; (e) 2.0; (f) 1.8; (g) 1.6; (h) 1.4. The printed direction of all samples is indicated by the white arrow in Figure (h).

While all samples printed at larger CD/LT (from 3.4 to 2.3) presented delamination, horizontal cracks and especially frequent vertical cracks, lower CD/LT produced samples with significantly

fewer cracks, with an almost complete disappearance of the vertical ones. The increase of CD/LT parameter induced an overcuring of the layers, making them stiffer and favouring the formation of multiple cracks, especially in the direction perpendicular to the printing one. However, even if a role of CD/LT on the structural integrity of the samples can be clearly stated, a well-defined correspondence between this ratio and the flexural strength cannot be established: **Figure 11(b)** shows in fact highly dispersed values (probably due to the still high defects concentration) even if a certain trend with higher strength for lower CD/LT values can be recognized.

As a following experimentation, a new batch of HA-2.7 samples was printed at CD/LT between 1.4 and 2.0, which lead to less defective structures. This time, before thermal treatment, water debinding was performed. As reported in literature, such strategy allows the removal of unpolymerized monomers, and creates open porosity which facilitates the subsequent resin burn-out [51,52]. This process led to a significant mass loss, of about 11%, while the printed dimensions showed a much less relevant variation (in the range between 0.2 to 1.0%). As a result, the water debinded samples showed a ~ 10% lower green density compared to the unwashed ones (see **Table 4**). In spite of this, samples still achieved a very high Archimedes density of the not-water debinded samples and 1-2% higher geometrical density, as provided by even fewer defective structures, as shown in **Figure 13**. In particular, comparing this microstructure to those reported in Figure 12, less edge cracks seems to be present. This improvement showed a further positive effect on the flexural strength, showing values closed to 100 MPa for the bars printed at the lowest CD/LT (1.4 and 1.6). This time, a clear correlation between flexural strength and CD/LT could be clearly stated, as shown in **Figure 11 (c)**, with best mechanical properties achieved at the ratio of 1.6.

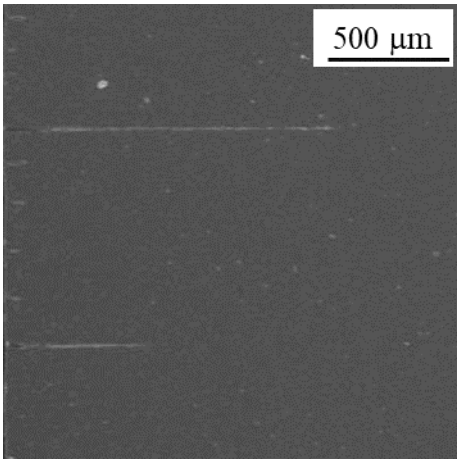

Figure 13: FESEM micrograph of HA-2.7 printed at CD/LT = 1.6 and submitted to water debinding prior to thermal debinding

3.6 Final optimization

The first part of work showed that using a powder with starting MPS of 0.91 μm or more is mandatory to eliminate major flaws in the printed bodies; the second part clearly indicates that CD/LT lower than 2 has to be selected to achieve high strength, being 1.6 the best ratio. In addition, a key role was played by water debinding before the thermal one, to reduce crack formation during polymer burn-out. Thus, a final optimization was performed at the previously mentioned CD/LT = 1.6, by joining water and thermal debinding. This procedure, successful for the slurry made by particles with MPS of 2.65 μm, was applied on slurries with progressively finer particles, and precisely on HA-1.7, HA-1.4 and HA-0.9, being this last the particle size limit determined before. Physical and mechanical results are collected in **Table 5**. Once again, we can observe a certain decrease of the green density, due to decreased solid loading of the slurry at increasing MPS. In spite of these, all samples reached very high Archimedes' density, and also high geometrical densities, in the range ~95-98%, strengthening again that the optimized conditions lead to less defective materials. At relatively fine particle sizes, such as 0.91 μm and 1.38 μm, the flexural strength was however still low, indicating a most important role of MPS compared to printing and debinding conditions. Best values were achieved for the HA-1.7 and HA-2.7 slurries, with a flexural strength higher than 100 MPa in the former case. For this last sample, a further test at the previous CD/LT equal to 2 was performed, showing a halving of the mechanical strength and further proving that a decrease of this ratio to 1.6 is mandatory to achieve very high mechanical properties.

Table 5: green, sintered density and flexural strength of printed bars, at different MPS and CD/LT values. For all of them, water and thermal debinding was performed

Slurry designation	CD/LT	Green density* (g/cm^3)	Archimedes density** (% TD)	Geometrical density** (%TD)	Mean flexural strength (MPa)
HA-0.9	1.6	1.85 ± 0.01	99.6 ± 0.3	95.3 ± 0.5	40 ± 7
HA-1.4	1.6	1.74 ± 0.01	98.8 ± 0.1	95.6 ± 0.2	62 ± 11
HA-1.7	1.6	1.78 ± 0.01	99.0 ± 0.3	97.6 ± 0.3	103 ± 6
HA-1.7	2.0	1.77 ± 0.02	99.2 ± 0.3	97.6 ± 0.2	47 ± 15
HA-2.7	1.6	1.64 ± 0.01	97.9 ± 0.5	96.9 ± 0.6	97 ± 13

*green density is intended as as-printed density (= resin and powder)
**Archimedes and geometrical densities are referred to theoretical density of HA equal to 3.156 g/cm^3

The density and mechanical resistance values determined in this work are among the highest found in the literature for hydroxyapatite-based bulk materials fabricated using DLP and stereolithography process. Kang et al. [55] produced hydroxyapatite disks by stereolithography and achieved the maximum Archimedes' density of 93.5% and biaxial flexural strength of ~ 7 MPa at optimum HA solid loading of 35vol%. Scalera et al. [11] used a 300 nm HA powder to prepare 60wt% solid loading slurries, providing sintered bars with a 3-point bending strength of 22 MPa. Yao et al. [32] used a ~ 4 μm-sized HA powder, to develop 40 vol% suspension. Bars fabricated by stereolithography achieved an Archimedes' density of 96% and 3-point bending strength of ~ 64 MPa, while this value increased to ~ 93 MPa when sintering was conducted under CO_2 atmosphere. Liu et al. [23] used a 12 μm-sized HA powder, and fabricated by DLP hydroxyapatite bars with Archimedes' density above 90% and flexural strength of 41 MPa.

Furthermore, the bending strength determined in this work was close to the best-reported results of 84.3–101.2 MPa with a relative density of 97.1%– 99% achieved through careful ceramic powder processing by traditional shaping methods and sintering [56].

4. Conclusion

Digital light processing (DLP) is a powerful method to fabricate advanced ceramics, such as hydroxyapatite (HA). However, some technique's intrinsic defects, due to both layered fabrication and debinding steps, drastically affect the structural integrity of bulk samples and related mechanical properties. This work demonstrates the key role played by some processing parameters in reducing – and in some cases completely eliminating - such flaws and enhancing the mechanical strength.

First, the role of HA mean particle size (MPS) was investigated. To this aim, different slurries were prepared starting from powders which differed in size by an order of magnitude, and precisely from 0.26 μm to 2.65 μm. While as-printed bars were highly compact and free from major flaws, thermal debinding induced the formation of delamination, horizontal, vertical and edge cracks whose extension and frequency decreased by increasing the starting MPS. In particular, a threshold corresponding to 0.9 μm MPS was established, indicating that micronic-sized powders are necessary for handling the sintered samples and achieving appreciable mechanical properties. This key result allows establishing a correlation between MPS and mechanical strength, as never performed for HA (and other advanced ceramics) processed by stereolithography and DLP techniques.

Second, the role of curing depth-to-layer thickness ratio (CD/LT) was studied, showing a progressive disappearance of major delamination and vertical cracks by decreasing this parameter, as a reduced overcuring of the layers results in reduced layer stiffness. An optimal ratio equal to 1.6 was determined, corresponding to maximum flexural strength.

Third, the role of debinding procedure was investigated, by comparing different sets of samples at the same MPS and CD/LT, but submitted to thermal debinding only or to a combination of water and thermal debinding steps. Polymer partial removal by water further decreased the cracks formation during the subsequent thermal debinding, especially the presence of edge cracks, and further enhanced the mechanical strength.

The final optimization joining all previous understanding allowed to fabricate samples with flexural strengths greater than 100 MPa. To the best of the authors' knowledge, these values are the highest achieved for stereolithography and DLP fabricated bulk HA samples, and are close to the best-reported results achieved through traditional shaping methods. Besides filing an important literature gap, this work paves the way for the future development of more complex hydroxyapatite structures, still at the best of their structural integrity and mechanical strength.

Acknowledgements

The authors gratefully acknowledge the Safety of Infrastructures and Constructions (SISCON) laboratory for providing the instrumentation for thermal and rheological analyses.

References

[1] J. Rödel, A.B.N. Kounga, M. Weissenberger-Eibl, D. Koch, A. Bierwisch, W. Rossner, M.J. Hoffmann, R. Danzer, G. Schneider, Development of a roadmap for advanced ceramics: 2010–2025. Journal of the European Ceramic Society 29 (2009) 1549–1560.

[2] Chen, Z., Sun, X., Shang, Y. et al. Dense ceramics with complex shape fabricated by 3D printing: A review. J Adv Ceram 10 (2021) 195–218.

[3] L. Wang and F Aldinger, Near-Net Shape Forming of Advanced Ceramics. Advanced Engineered Materials 2 [3] (2000) 110-113.

[4] Z. Chen, Z. Li, J. Li, C. Liu, C. Lao, Y. Fu, C. Liu, Y. Li, P. Wang, Y. He. 3D printing of ceramics: A review. Journal of the European Ceramic Society 39 (2019) 661-687.

[5] Rasaki, S.A., Xiong, D., Xiong, S. et al. Photopolymerization-based additive manufacturing of ceramics: A systematic review. J Adv Ceram 10 (2021) 442–471.

[6] F. Doreau, C. Chaput, T. Chartier. Stereolithography for Manufacturing Ceramic Parts. Advanced Engineered Materials 2 [8] (2000) 493-496.

[7] C.-J. Bae and J.W. Halloran, Influence of Residual Monomer on Cracking in Ceramic Fabricated by Stereolithography. Int. J. Appl. Ceram. Technol., 8 [6] (2011) 1289–1295.

[8] E. Johansson, O. Lidström, J. Johansson, O. Lyckfeldt and E. Adolfsson, Influence of Resin Composition on the Defect Formation in Alumina Manufactured by Stereolithography. Materials 10 (2017) 138-148.

[9] H.-I Hsiang, C.-Y. Lee, C.-C. Chen, J. Wang, D. Tang, Z. Dong, Polycrystalline alumina ceramic fabrication using digital stereolithographic light process. Ceramics International 47 (2021) 33815–33826.

[10] L. Ferrage, G. Bertrand, P. Lenormand, D. Grossin1, B. Ben-Nissan, A review of the additive manufacturing (3DP) of bioceramics: alumina, zirconia (PSZ) and hydroxyapatite. J Aust Ceram Soc (2017) 53:11–20

[11] F. Scalera, C. Esposito Corcione, F. Montagna, A. Sannino, A. Maffezzoli, Development and characterization of UV curable epoxy/hydroxyapatite suspensions for stereolithography applied to bone tissue engineering. Ceramics International 40 (2014) 15455–15462.

[12] C. Feng, K. Zhang, R. He, G. Ding, M. Xia, X. Jin, C. Xie, Additive manufacturing of hydroxyapatite bioceramic scaffolds: Dispersion, digital light processing, sintering, mechanical properties, and biocompatibility. Journal of Advanced Ceramics 9 (2020) 360–373.

[13] C. Schmidleithner, S. Malferrari, R. Palgrave, D. Bomze, M. Schwentenwein and D.M. Kalaskar, Application of high resolution DLP stereolithography for fabrication of tricalcium phosphate scaffolds for bone regeneration. Biomed. Mater. 14 (2019) 045018.

[14] Z. Wang, C. Huang, J. Wang, B. Zhou, C.A. Abbas, X. Wang, Design and Characterization of hydroxyapatite scaffolds fabricated by stereolithography for bone tissue engineering applications. Procedia CIRP 89 (2020) 170-175.

[15] L. L. Hench, An introduction to bioceramics, second edition, Imperial College Press, 2013.

[16] S. V. Dorozhkin, “Calcium orthophosphate bioceramics,” Ceramics International, 41 (2015) 13913-13966.

[17] J.A. Letta, M. Sundareswari, K. Ravichandran, Porous hydroxyapatite scaffolds for orthopedic and dental applications - the role of binders. Materials Today: Proceedings 3 (2016) 1672–1677.

[18] H. Oonishi, Orthopaedic applications of hydroxyapatite. Biomaterials 12 [2] (1991) 171-178.

[19] R. Petit, The use of hydroxyapatite in orthopaedic surgery: A ten-year review. European Journal of Orthopaedic Surgery & Traumatology volume 9 (1999) 71–74.

[20] S. Balhuc, R. Campian, A. Labunet, M. Negucioiu, S. Buduru, A. Kui, Dental Applications of Systems Based on Hydroxyapatite Nanoparticles—An Evidence-Based Update. Crystals 11 [6] (2021) 674-692.

[21] G. Carotenuto, G. Spagnuolo, L. Ambrosio, L. Nicolais, Macroporous hydroxyapatite as alloplastic material for dental applications. Journal of Materials Science: Materials in Medicine 10 (1999) 671–676.

[22] X. Li, Y. Yuan, L. Liu, Y.-S. Leung, Y. Chen. Y. Chen, 3D printing of hydroxyapatite/tricalcium phosphate scaffold with hierarchical porous structure for bone regeneration. Bio-Design and Manufacturing (2020) 3:15–29

[23] Z. Liu, H. Liang, T. Shie, D. Xiem R. Chen, X. Han, L. Shen, C. Wang, Z. Tian, Additive manufacturing of hydroxyapatite bone scaffolds via digital light processing and in vitro compatibility. Ceramics International 45 (2019) 11079–11086

[24] R. Liu, L. Ma, H. Liu, B. Xu, C. Feng, R. He, Effects of pore size on the mechanical and biological properties of stereolithographic 3D printed HAp bioceramic scaffold. Ceramics International 47 (2021) 28924–28931

[25] F. Baino, G. Magnaterra, E. Fiume, A. Schiavi, L.-P. Tofan, M. Schwentenwein, E. Verné, Digital light processing stereolithography of hydroxyapatite scaffolds with bone-like architecture, permeability, and mechanical properties. Journal of the American Ceramic Society, 2021;00:1–10.

[26] Q. Chen, B. Zou, Q. Lai, Y. Wang, R. Xue, H. Xing, X. Fu, C. Huang, P. Yao, A study on biosafety of HAP ceramic prepared by SLA-3D printing technology directly. Journal of the Mechanical Behavior of Biomedical Materials 98 (2019) 327–335

[27] C. Feng, K. Zhang, R. He, G. Ding, M. Xia, X. Jin, C. Xie, Additive manufacturing of hydroxyapatite bioceramic scaffolds: Dispersion, digital light processing, sintering, mechanical properties, and biocompatibility. Journal of Advanced Ceramics 2020, 9(3): 360–373.

[28] L. Le Guéhennec, D. Van hede, E. Plougonven, G. Nolens, B. Verlée, M.-C. De Pauw, F. Lambert, In vitro and in vivo biocompatibility of calcium-phosphate scaffolds three-dimensional printed by stereolithography for bone regeneration. J Biomed Mater Res. 2020;108A:412–425.

[29] C. Schmidleithner, S. Malferrari, R. Palgrave, D. Bomze, M. Schwentenwein, D.M. Kalaskar, Application of high resolution DLP stereolithography for fabrication of tricalcium phosphate scaffolds for bone regeneration. Biomed. Mater. 14 (2019) 045018

[30] F. Scalera, C. Esposito Corcione, F. Montagna, A. Sannino, A. Maffezzoli, Development and characterization of UV curable epoxy/hydroxyapatite suspensions for stereolithography applied to bone tissue engineering. Ceramics International 40 (2014) 15455–15462.

[31] Y. Wei, D. Zhao, Q. Cao, J. Wang, Y. Wu, B. Yuan, X. Li, X. Chen, Y. Zhou, X. Yang, X. Zhu, C. Tu, X. Zhang, Stereolithography-Based Additive Manufacturing of High-Performance Osteoinductive Calcium Phosphate Ceramics by a Digital Light-Processing System. ACS Biomater. Sci. Eng. 6 (2020) 1787−1797

[32] Yao, Y., Qin, W., Xing, B. et al. High performance hydroxyapatite ceramics and a triply periodic minimum surface structure fabricated by digital light processing 3D printing. J Adv Ceram 10 (2021) 39–48.

[33] S. Raynaud, E. Champion, D. Bernache- Assollant and J. Laval, “Determination of calcium/phosphorus atomic ratio of calcium phosphate apatites using x-ray diffractometry,” Journal of the American Ceramic Society 84 (2004) 359-366.

[34] Mohammadi, M.; Tulliani, J.-M.; Montanaro, L.; Palmero, P. Gelcasting and sintering of hydroxyapatite materials: Effect of particle size and Ca/P ratio on microstructural, mechanical and biological properties. J. Eur. Ceram. Soc. 41 (2021) 7301–7310.

[35] B. Coppola, J. Schmitt, T. Lacondemine, C. Tardivat, L. Montanaro, P. Palmero, Digital light processing stereolithography of zirconia ceramics: Slurry elaboration and orientation-reliant mechanical properties. Journal of the European Ceramic Society 42 (2022) 2974-2982

[36] B. Coppola, T. Lacondemine, C. Tardivat, L. Montanaro, P. Palmero, Designing alumina-zirconia composites by DLP-based stereolithography: Microstructural tailoring and mechanical performances. Ceramics International 47 (2021) 13457-13468

[37] Liang, W., Xu, Y., Huang, Y., Yariv, A., Fleming, J. G., & Lin, S. Y. (2004). Mie scattering analysis of spherical Bragg “onion” resonators. Optics Express, 12 (2004) 657-669.

[38] J.W. Halloran, Ceramic Stereolithography: Additive Manufacturing for Ceramics by Photopolymerization. Annual Review of Materials Research 46 (2016) 19–40.

[39] A.C. Uzcategui, A. Muralidharan, V.L. Ferguson, S.J. Bryant, R.R. McLeod, Understanding and Improving Mechanical Properties in 3D printed Parts Using a Dual-Cure Acrylate-Based Resin for Stereolithography. Adv Eng Mater. 20 (2018) 1800876.

[40] M. Mohammadi, J.-M. Tulliani and P. Palmero, Fabrication of dense and porous biphasic calcium phosphates: Effect of dispersion on sinterability and microstructural development, International Journal of Applied Ceramic Technology, 16 (2019) 1797-1806.

[41] Knowles, J. C., Callcut, S., & Georgiou, G. (2000). Characterisation of the rheological properties and zeta potential of a range of hydroxyapatite powders. Biomaterials, 21 (13) 1387-1392.

[42] R.P. Chhabra and J.F. Richardson, Non-Newtonian Flow and Applied Rheology, Elsevier Ltd, second edition, 2008.

[43] L. Xing-Bang, Z. He, Z. Jing-Xian, D. Yu-Sen, J. Dong-Liang, Powder Characteristics on the Rheological Performance of Resin-based Zirconia Suspension for Stereolithography. Journal of Inorganic Materials, 35 (2) 2020.

[44] C.J. Bae, A. Ramachandran, K. Chung, S. Park, Ceramic stereolithography: additive manufacturing for 3D complex ceramic structures, J. Korean. Ceram. Soc. 54 (2017) 470–477.

[45] Z. Wang, C. Huang, J. Wang, B. Zou, Development of a novel aqueous hydroxyapatite suspension for stereolithography applied to bone tissue engineering, Ceram. Int. 45 (2019) 3902–3909.

[46] Lasgorceix M, Champion E, Chartier T. Shaping by microstereolithography and sintering of micro-porous silicon substituted hydroxyapatite. Journal of the European Ceramic Society, 36 (2016) 1091-1101.

[47] C. Hinczewski, S. Corbel, T. Chartier, Ceramic suspensions suitable for stereolithography, J. Eur. Ceram. Soc 18 (1998) 583–590.

[48] H. Liao, Stereolithography using Compositions Containing Ceramic Powders, PhD thesis, University of Toronto, 1998.

[49] Licciulli, A., Corcione, C. E., Greco, A., Amicarelli, V., & Maffezzoli, A. (2005). Laser stereolithography of ZrO_2 toughened Al_2O_3. Journal of the European Ceramic Society, 25 (2005) 1581-1589.

[50] Spierings, A. B., Schneider, M. U., & Eggenberger, R. (2011). Comparison of density measurement techniques for additive manufactured metallic parts. Rapid Prototyping Journal, 17 (2011) 380-386.

[51] Wang, K., Qiu, M., Jiao, C., Gu, J., Xie, D., Wang, C., ... & Shen, L. Study on defect-free debinding green body of ceramic formed by DLP technology. Ceramics International, 46 (2020) 2438-2446.

[52] Li, H., Liu, Y., Liu, Y., Zeng, Q., Hu, K., Lu, Z., ... & Li, J. (2021). Influence of debinding holding time on mechanical properties of 3D-printed alumina ceramic cores. Ceramics International, 47 (2021) 4884-4894.

[53] Putlyaev, V.I., Evdokimov, P.V., Safronova, T.V., Klimashina, E., & Orlov, N.K. Fabrication of osteoconductive $Ca_3–xM_{2x}(PO_4)_2$ (M = Na, K) calcium phosphate bioceramics by stereolithographic 3D printing. Inorganic Materials, 53 (2017) 529-535.

[54] Knapp, A.M. and Halloran, J.W. Binder Removal from Ceramic-Filled Thermoplastic Blends. Journal of the American Ceramic Society, 89 (2006) 2776-2781.

[55] J.-H. Kang, K. Sakthiabirami, K.-J. Jang, J.-G. Jang, G.-J. Oh, C. Park, J.G. Fisher, S.-W. Park, Mechanical and biological evaluation of lattice structured hydroxyapatite scaffolds produced via stereolithography additive manufacturing. Materials & Design 214 (2022) 110372.

[56] Rapacz-Kmita A, Ślósarczyk A, Paszkiewicz Z. Mechanical properties of HAp–ZrO_2 composites. J Eur Ceram Soc. 26 (2006) 1481–1488.